Laminated Metal Composites by Infiltration

ARDA ÇETIN, JÉRÔME KREBS, ALEXANDRE DURUSSEL, ANDREAS ROSSOLL, JUNYA INOUE, TOSHIHIKO KOSEKI, SHOICHI NAMBU, and ANDREAS MORTENSEN

We show that steel-magnesium alloy laminated metal composites (LMCs) can be produced by gas pressure infiltration of a liquid magnesium alloy between layers of stacked dimpled steel sheets. Resulting LMCs are amenable to subsequent warm rolling. The LMCs are free of pores or brittle intermetallics and feature, in the as-cast condition, metal layers of uniform thickness and spacing. The ultimate tensile strength of the as-cast LMCs, of 260 MPa, obeys the ''rule-of-mixtures'' (ROM). The uniform tensile elongation, of around 20 pct, makes the infiltrated LMC nearly as ductile as the bulk steel it contains, implying that the magnesium alloy in the as-cast LMCs has a substantially increased tensile ductility in comparison to its metallurgically equivalent bulk state. Rolling reduces the metal layer thicknesses, causes waviness in the interface, and makes the LMCs stronger but less ductile, by factors in the vicinity of 2 for both properties; the main cause for this is work hardening in the steel layers.

DOI: 10.1007/s11661-011-0756-2

I. INTRODUCTION

LAMINATED metal–(metal) composites (LMCs) are made by bonding layers of two or more alternating metals. These are some of the oldest composites known to man: lamination has been used for well over a millennium by blacksmiths to combine strength with ductility in steel.[1–4]

One of the most attractive and interesting attributes of LMCs is their ductility. If one combines two ductile metals that both fail in tension by necking, then the laminated composite will not fail at the necking strain of its less ductile phase. Rather, it will start necking at a strain higher than that, the value of which depends in nontrivial fashion on the properties and relative proportion of the two bonded metals. The reason is that, if the two phases are strongly bonded together, the more ductile layers prevent necking in the other, less ductile, metal, thus ''coaxing'' the latter to deform well beyond the peak tensile strain that it would reach alone.[2–11] In some cases, the tensile elongation of laminated composites can even exceed the ''rule-of-mixtures'' (ROM) volume average of ductilities displayed by individual phases making the composite.[2,3]

Lamination is therefore a strategy by which one may drive certain metals and alloys to deform in tension well beyond their normal performance range. An example is with martensitic steel, which, despite its inherent brittleness, can, in a laminated composite, experience tensile strains as high as 20 pct.[10,11] Magnesium alloys also tend to exhibit relatively poor tensile ductility; therefore, lamination may be an attractive strategy toward improving its performance in structural applications, particularly where deformability is required. To this end, magnesium should be combined with another, more ductile, metal; steel is attractive in this regard, because it is often ductile and also because magnesium is sufficiently inert in contact with iron (magnesium is generally melted in steel crucibles).[12,13] There are, thus, published explorations of composite structures combining steel with magnesium and examining the chemical compatibility between iron and magnesium alloys;[4,14,15] however, none to the best of our knowledge concerns laminated structures.

We present here a first exploration of the processing and properties of laminated composites combining a magnesium alloy with mild steel. There are many ways to manufacture LMCs; these can be classified into bonding- or deposition-based methods. Bonding methods include a wide array of processes such as roll bonding, diffusion bonding, adhesive bonding, melt bonding, reaction bonding, deformation bonding, brazing, and soldering.[2] Deposition methods, unless combined with bonding methods, produce two- or three-layer structures, and mainly include sputtering, physical and chemical vapor deposition, electroplating, and cocasting.[2] On the other hand, infiltration seldom has been explored as a method to make metal-(metal) laminates; it has the advantage of relative speed,

ARDA ÇETIN, Postdoctoral Researcher, JÉRÔME KREBS, PhD Student, ANDREAS ROSSOLL, Scientist, and ANDREAS MORTENSEN, Professor, are with Ecole Polytechnique Fédérale de Lausanne (EPFL), Laboratory of Mechanical Metallurgy, CH-1015 Lausanne, Switzerland. Contact e-mail: arda.cetin@epfl.ch ALEXANDRE DURUSSEL, PhD Student, formerly with Ecole Polytechnique Fédérale de Lausanne (EPFL), Laboratory of Mechanical Metallurgy, and Department of Materials Engineering, The University of Tokyo, Bunkyo-ku, Tokyo 113-8656, Japan, is now with Ecole Polytechnique Fédérale de Lausanne (EPFL), Computational Materials Laboratory. JUNYA INOUE, Associate Professor, TOSHIHIKO KOSEKI, Professor, and SHOICHI NAMBU, Assistant Professor, are with the Department of Materials Engineering, The University of Tokyo.

Manuscript submitted December 17, 2010.
Article published online June 18, 2011

coupled with the fact that, unlike most solid-state bonding methods such as colamination, the process introduces no work hardening of the more refractory phase, thus preserving its formability.[16] In what follows, we demonstrate how infiltration can be used in the production of laminated composites and explore the structure and tensile properties of infiltrated laminated composites combining magnesium with steel sheet.

II. EXPERIMENTAL PROCEDURES

A. *Materials*

The LMCs combined a ductile cold-rolled low-carbon steel (SPCC steel, Japanese standard JIS G3141) with ZM21 magnesium alloy, a zinc and manganese-containing wrought magnesium alloy. The SPCC steel sheets were cold rolled from 0.6-mm-thick steel sheets down to 0.1 or 0.2 mm. The elemental composition of the two constituent alloys is given in Table I.

ZM21 alloy was chosen because it contains two elements (Mn and Zn) known for their good compatibility with steel and is free of other traditional alloying elements known to form brittle intermetallics in contact with iron, such as Al (which leads to the formation of compounds such as $Fe_2(Al,Mg)C$[14] and $Al_5Fe_2(Zn)$[15]).

B. *Making LMCs by Infiltration*

The approach we used broadly consists of stacking steel sheets with a uniform spacing and infiltrating the stack with a liquid Mg alloy, followed by solidification of the Mg alloy between the steel layers. In this, a key challenge is to maintain the (thin and, hence, flexible) steel sheets straight and separate; to this end, we punched small dimples into the steel sheets. Resulting protrusions keep the steel sheets apart at discrete locations, sufficiently small and remote not to strongly influence laminate tensile properties (as will be seen subsequently), yet sufficiently close for the steel sheets to remain straight during the infiltration process (Appendices A and B).

To prepare the stacks, steel sheets were ground to clean and smoothen their surface and then cut to desired dimensions (28×100 mm^2) using automatic shears. Steel pieces 40×60 mm^2 wide were also cut to make LMCs for subsequent rolling.

The steel sheets were then punched to produce the dimples and stacked. To this end, a small device including a punch, two aluminum plates (one upper and one lower), pins, and bolts was assembled to introduce the dimples reproducibly (Appendix A). The upper plate contains cylindrical holes 1.02 mm in diameter, while the lower plate has matching conical indentations, 1 mm in diameter and 0.5-mm deep. The depth of the dimples is tailored by altering the length of the punch relative to the upper plate thickness; this was adjusted such that the resulting height of the dimples was equal to the layer thickness, thus producing a 1:1 thickness ratio between the alternating layers in the resulting LMC. The depth of the dimples was checked with a micrometer, accepting a tolerance of 0.05 mm. Finally, the dimpled sheets were stacked to make the layered steel preform, which was infiltrated with ZM21 magnesium alloy. Note that the upper plate is designed in such a way that the position of the holes be asymmetric along its length (Figure A2). Therefore, one can prevent alignment of the dimples of alternating steel layers by simply rotating the sheets by 180 deg when stacking these. The free distance between the dimples was chosen based on an estimation of the bending stresses acting on the steel sheets during infiltration; the estimation is given in Appendix B.

The LMCs were produced with two different dimple configurations. In the first group, the sheets were punched in such a way that the dimples be positioned within the gage section of tensile specimens machined from the LMCs. This configuration is identified as the *dimpled* configuration in the following. The second group, in which the dimples were positioned outside the tensile bar gage section, is identified as the *nondimpled* configuration. This distinction is made to assess the extent to which the dimples affect the mechanical properties of the LMCs. Table II summarizes the arrangement of the dimples and the laminate dimensions.

Infiltration was carried out in a steel crucible coated with boron nitride spray (Sindlhauser Materials GmbH, Kempten, Germany) placed within a pressure vessel. The stacked preform was infiltrated with ZM21 alloy, superheated to 983 K (710 °C), by applying Ar gas up to a maximum pressure of 0.2 MPa for 15 minutes, after initial evacuation of the preform using a mechanical pump.

C. *Rolling*

The LMCs made from 40×60 mm^2 steel sheets were rolled using a Sandoz & Co. (La Chaux-de-Fonds, Switzerland) laboratory-scale rolling mill, having a roll diameter of 10.5 cm. The samples were held at 523 K (250 °C) for 30 minutes prior to rolling and reheated at that temperature for 10 minutes between the passes. The rolls were heated with hot air to a surface temperature around 343 K (70 °C). The samples were rolled in four passes to a thickness reduction of 16 pct per pass to reach a total thickness reduction between 50 and 55 pct. The rolling speed was 10 cm/s. The rolled samples were

Table I. Elemental Composition (Weight Percent) of Constituent Materials

	C	Si	Mn	P	S	Zn	Mg	Fe
SPCC steel	0.04	0.01	0.017	0.013	0.010	—	—	balance
ZM21 (nominal)	—	—	1	—	—	2	balance	—

Table II. Summary of the Laminate Dimensions and Dimple Arrangements

Thickness of the Steel Sheets (mm)	Width × Length (mm × mm)	Number of Steel Layers	Expected Thickness after Infiltration (mm)	Dimpled	Schematic of the Dimple Arrangement
0.1	28 × 100	11	2.1	no	Fig. A3(a)
		11	2.1	yes	Fig. A3(b)
	40 × 60	12	2.3	no	Fig. A3(c)
		12	2.3	yes	Fig. A3(d)
0.2	28 × 100	6	2.2	no	Fig. A2(a)
		6	2.2	yes	Fig. A2(b)
	40 × 60	10	3.8	no	Fig. A2(a)
		10	3.8	yes	Fig. A2(b)

finally annealed at 723 K (450 °C) for 2 hours under Ar atmosphere. For simplicity, in what follows, the samples are always designated with reference to the original layer thickness prior to rolling (*i.e.*, "0.2-mm rolled" and "0.1-mm rolled"). Maximum strains that could be reached in warm rolling were on the order of 60 pct; at deformations higher than that, the LMCs tended to debond.

D. *Tensile Tests and Microhardness*

Flat dog-bone tensile specimens (ASTM standard E8M), with gage dimensions of 25 mm × 6 mm and a thickness of 1 to 2.2 mm depending on the process history (rolled or as-cast), were machined from infiltrated LMCs. Tensile samples were also produced and tested from (1) a 1-mm-thick SPCC steel sheet having undergone a thermal treatment identical to the thermal history of the infiltrated steel stacks; and (2) cast ZM21 alloy rectangular plates, 2-mm thick. Rolled LMCs were tested along their rolling direction. Note that these sample gage lengths are slightly too short to perfectly meet the tensile stress conditions in the bars; this adds some uncertainty to the data.

All tests were run on a Zwick (Ulm, Germany) screw-driven machine with a 10-kN load cell at a nominal strain rate of 6×10^{-4} s^{-1}. Longitudinal displacements were measured with a double-sided clip-on extensometer having a gage length between 8 and 10 mm. It should be noted that this gage length is shorter than the 25-mm sample gage length, such that the recorded fracture strain depends on the location of the neck once instability sets in. Uncertainty on stress is estimated (based mostly on uncertainty on the cross-sectional area) to be ± 3 MPa, while uncertainty on elongations is estimated at ± 0.7 pct. The Vickers microhardness of steel and ZM21 layers within the LMCs, in as-cast and rolled states, was measured using a Shimadzu HMV-2000 microhardness instrument (Tokyo).

E. *Microstructural Characterization and Fractography*

Microstructural features of the LMCs at various stages of processing were characterized using an optical microscope, a scanning electron microscope (SEM) (Philips XLF30, Eindhoven, The Netherlands), and electron backscatter diffraction (EBSD) analysis (TSL Solutions, Kanagawa, Japan). Fracture surfaces were also examined in the SEM. Samples being pore free, the volume fractions of steel and magnesium alloy in the LMCs were measured by densitometry, using a Sartorius MC 210P microbalance and a Sartorius Gravity Determination Kit YDK0.1 (IG Instrumenten-Gesellschaft, Zurich, Switzerland).

III. RESULTS AND DISCUSSION

A. *Laminate Structure*

Figure 1 presents the microstructure of as-cast LMCs made using (a) 0.2 mm and (b) 0.1-mm-thick steel sheets, respectively. As seen, the stacks are well infiltrated and free of porosity. Also, the steel sheets did not bend during infiltration and the reproducibility of the thickness of ZM21 alloy layers was satisfactory. The volume fraction of steel deduced by densitometry is near 50 pct; this is only slightly lower than the value expected were the dimples to hold steel plates apart by a distance strictly equal to the steel plate thickness (nearer 53 pct).

Figure 2 presents a comparison of the grain structure in the SPCC steel before and after infiltration, showing that the elongated grain structure of the cold-rolled SPCC steel (Figure 2(a)) recrystallized into a fine-grained, equiaxed microstructure during infiltration (mean grain size = 12 μm, Figure 2(b)). ZM21 alloy grains, on the other hand, were large, on the order of millimeters and, hence, well above the laminate layer thickness. Figure 3 shows the large grain size in a ZM21 layer together with the local orientation of grains. Monolithic ZM21 samples cast for tensile testing had a similar grain size, on the order of millimeters. No second phase was detected in the ZM21 layers. Statistically significant grain size data were thus difficult to obtain, as were conclusive texture data, since each layer is composed of only a few grains.

Typical microstructures of the rolled LMCs are given in Figure 4, corresponding to (a) 0.2- and (b) 0.1-mm initial layer thicknesses, respectively. Rolled samples also display a sound and crack-free interface, free of any brittle reaction products. The grain structure of ZM21 layers was refined after rolling and subsequent annealing at 723 K (450 °C) (Mg grain sizes were roughly 60 and 40 μm for 0.2- and 0.1-mm layer thickness, respectively), with signs of recrystallization. Figure 5 shows the {0001} pole figures of ZM21 layers in the rolled LMCs. As seen, almost all *c*-axes of Mg grains in both LMCs

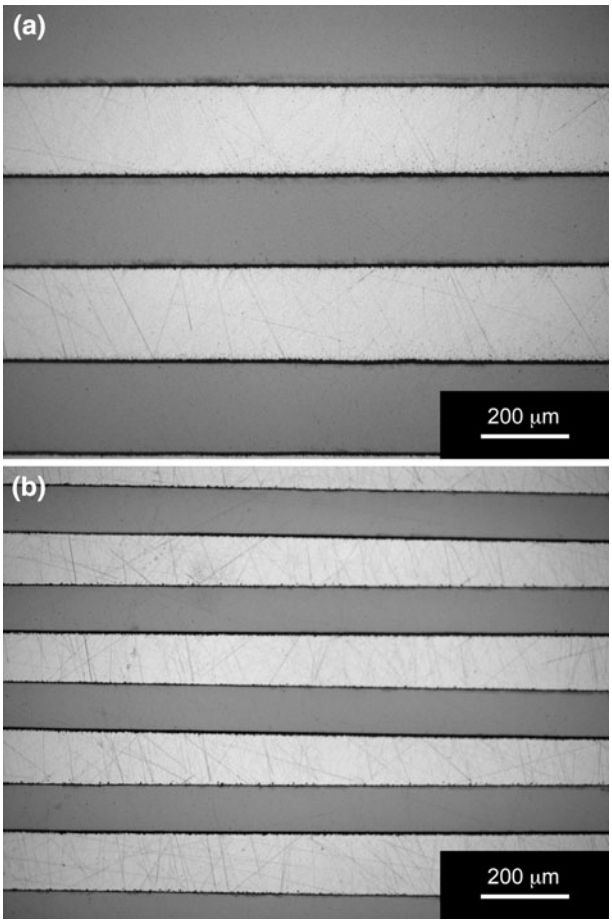

Fig. 1—Optical micrographs of as-cast LMCs with (*a*) 0.2-mm and (*b*) 0.1-mm layer thickness. The dark phase is steel and the light phase is ZM21.

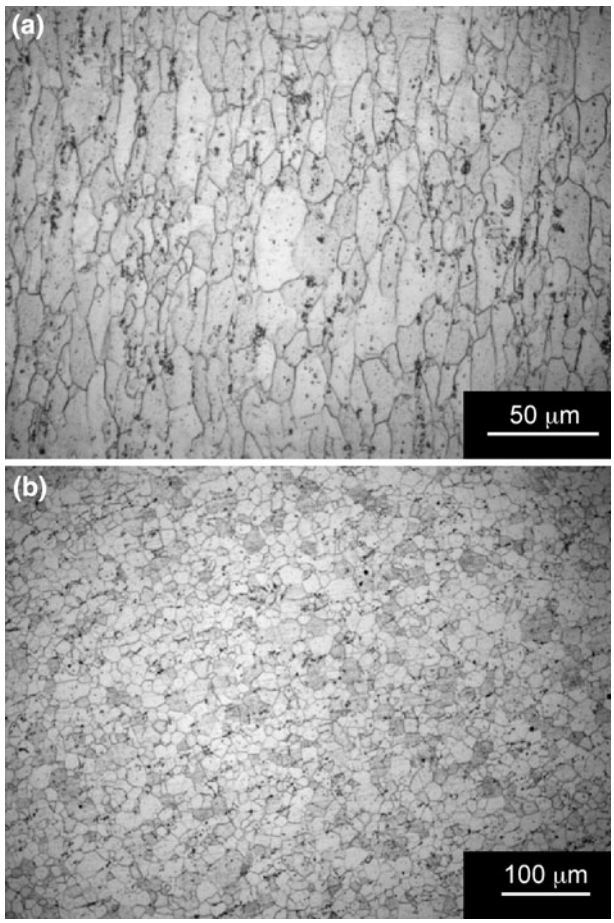

Fig. 2—Grain structure of the SPCC steel (*a*) before and (*b*) after infiltration. The elongated grain structure of the steel recrystallizes into an equiaxed structure, with a mean grain size of 12 μm.

are aligned parallel to the rolling direction (which, as mentioned, was also the tensile axis of the rolled samples).

B. *Interface*

The interface is free of pores and reveals no intermetallic compounds. Figure 6 presents EDX line scan profiles in the close vicinity of the interface of as-cast LMCs. There is no segregation of Fe or Mg at the interface, nor of Zn, which is the principal alloying element of ZM21 alloy. On the other hand, there is marked segregation of Mn, seemingly coming from the ZM21 alloy, both at the interface and within the steel (Figure 6).

Mn is added to Mg-Zn alloys mainly to improve their corrosion resistance.[17] The microstructure of cast ZM series alloys generally shows a coarse grain size, due to the lack of any grain refining elements (as do cast bulk ZM21 tensile samples of this work, as previously discussed). In the alloy, Mn is present in the form of particles since it has essentially no solubility in solid Mg.[18]

EDX line scans through the interface of the LMCs reveal that Mn migrates toward Fe in liquid Mg and

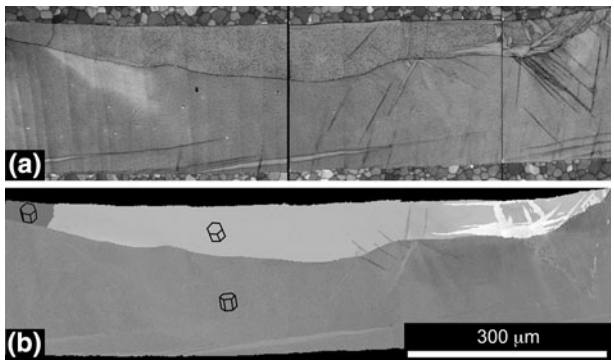

Fig. 3—(*a*) Assembly of SEM micrographs of a ZM21 layer in an as-cast sample after tensile testing, (*b*) together with its grain orientation image. Note the large grain size, together with the presence of deformation twins.

then penetrates over a limited depth into the steel plates. EDX line scan profiles indicate that Mn penetration into steel is somewhat deeper compared to the thickness of Mn that stays on the Mg alloy side, with no difference visible in the depth of penetration between the two steel plate thickness values (Figure 6). During solidification, the remaining Mn in the Mg alloy side precipitates as

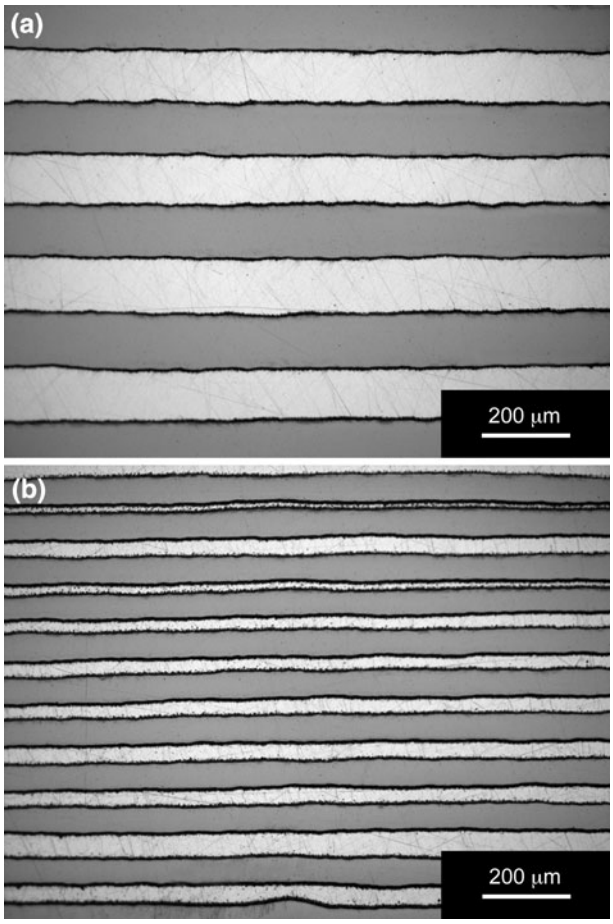

Fig. 4—Micrographs of rolled LMCs with (*a*) 0.2-mm and (*b*) 0.1-mm layer thickness. The dark phase is steel and the light phase is ZM21.

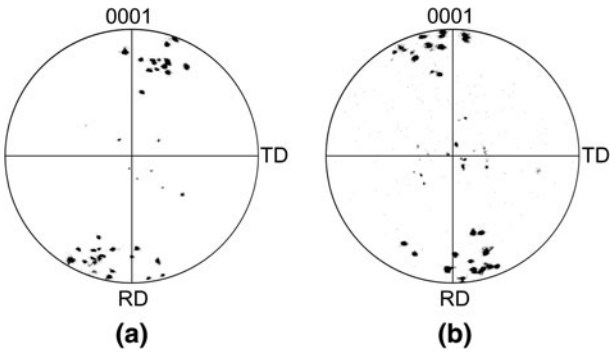

Fig. 5—{0001} pole figures of ZM21 layers in the rolled LMCs with (*a*) 0.2-mm and (*b*) 0.1-mm initial layer thickness.

Mn-rich particles (these are too small to be visible at the magnification of Figure 3).

C. *Tensile Behavior of the As-Cast LMCs*

Table III lists the mechanical properties of the constituent materials: E is the Young's modulus, $\sigma_{0.2}$ is the proof stress, UTS is the ultimate tensile strength, and ε_u is the peak uniform true strain, computed where the engineering stress-strain curves reach their maximum.

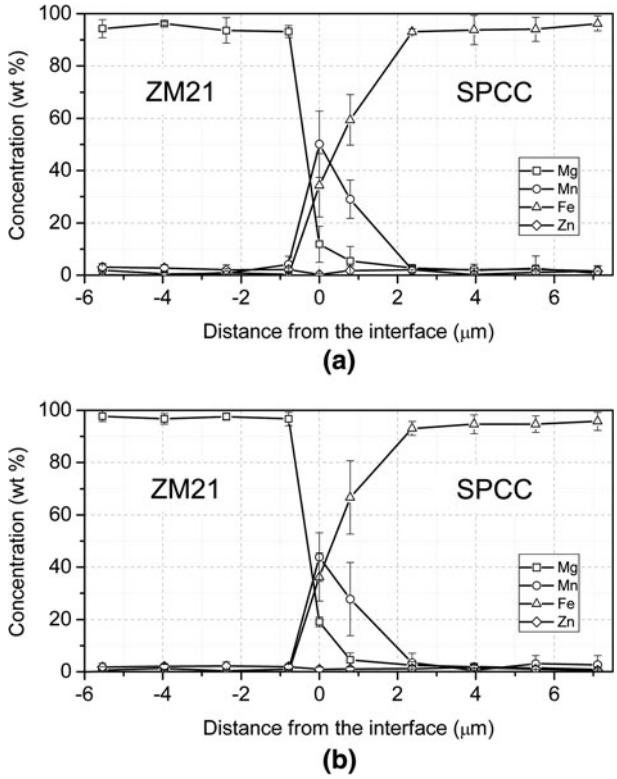

Fig. 6—Averaged EDX line scans through the interface of (*a*) 0.2-mm and (*b*) 0.1-mm as-cast LMCs. There is a clear segregation of Mn at the interface in both samples.

Table III. Mechanical Properties of Monolithic SPCC Steel and ZM21 Alloy

Material	E (GPa)	$\sigma_{0.2}$ (MPa)	UTS (MPa)	ε_u (Pct)
SPCC steel	200	260	320	25.7
As-cast ZM21	45	131	225	13.7

Tensile tests were conducted on two samples per condition. Results, together with the corresponding steel volume fraction within the LMCs (V_{SPCC}), are given in Table IV, where Z denotes the percent reduction in area at fracture in the neck. Four typical tensile curves, two for as-cast and two for rolled LMCs, are plotted in Figure 7. As seen from the data, the presence of dimples in the steel sheets does not affect noticeably the proof or ultimate tensile strength of the LMCs, either in as-cast or in rolled conditions. An influence of the dimples on either the peak uniform strain, ε_u, or on the local reduction in area at fracture, Z, is also hard to detect: variations in Z from sample to sample, or between batches with and without dimples, are both around 7 pct. Overall, thus, dimples that were introduced in the steel sheets to keep them apart during infiltration do not, in the present data, exert an influence that could be detected in tensile properties of the resulting LMCs.

Table IV. Tensile Properties of Infiltrated Steel/Magnesium Alloy LMCs (by Sample)

$t_{initial}$ (mm)	Processing History	Dimpled	V_{SPCC} (Pct) ± 0.1 Pct	$\sigma_{0.2}$(MPa) ± 3 MPa	UTS (MPa) ± 3 MPa	ε_u (Pct) ± 0.7 Pct	$\varepsilon_{u,th}$ (Pct)	Z (Pct) ± 1 Pct
0.1	as-cast	no	46.1	198	260	19.0	21.8	38
			46.6	200	259	17.9	21.9	38
		yes	48.6	201	266	19.4	22.1	36
			48.1	183	265	24.1	22.0	40
	rolled	no	46.0	308	366	6.5	—	19
			44.6	310	360	6.6	—	20
		yes	46.9	328	374	6.7	—	22
			47.9	329	371	5.5	—	16
0.2	as-cast	no	52.5	209	263	22.4	22.5	42
			52.1	233	261	22.2	22.4	39
		yes	50.4	198	264	17.2	22.3	28
			50.8	197	263	16.9	22.3	35
	rolled	no	51.5	349	386	6.2	—	26
			50.5	334	385	8.0	—	29
		yes	49.5	336	380	8.9	—	20
			50.0	337	381	8.0	—	19

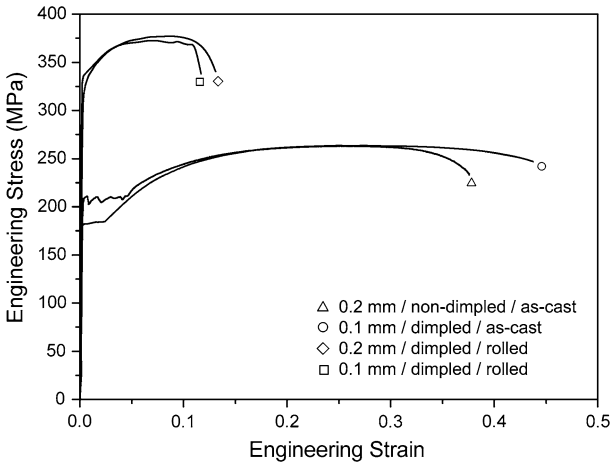

Fig. 7—Typical uniaxial engineering stress-strain curves of as-cast and rolled LMCs, for each of the two layer thicknesses explored.

The Young's modulus E_c of the present LMCs was roughly 130 GPa for all present composites (E_c deduced from stress-strain curves; uncertainty in E_c is, hence, too high to capture variations that result from small variations in relative phase volume fractions). This corresponds roughly to the equistrain rule-of-mixtures, in that this value is near the average of the tensile moduli of the SPCC steel and the ZM21 phases, both present in roughly equal proportions in the composites produced here.

UTS values of all as-cast samples are within 95 to 98 pct of ROM predictions (a corresponding assessment is difficult to make for the rolled LMCs, given the lack of data on mechanical properties of rolled constituent phases). The specific proof stress (stress divided by density) of the as-cast LMCs is found to be around 40 ± 2 kN·m/kg (varying with the small variations in V_{SPCC}). This value indicates an improvement by 21 pct in the specific proof stress over SPCC steel (33 kN·m/kg) after lamination with the magnesium alloy. The improvement is more pronounced for rolled samples (94 pct), which have a specific proof stress around 64 kN·m/kg. The strength enhancement due to rolling is, however, offset by a lower ductility, as expected, since the higher strength is mostly due to cold work in the steel.

Noting that the specific UTS of the SPCC steel is 41 kN·m/kg, the corresponding improvements in specific UTS are 29 and 86 pct (52 and 76 kN·m/kg) for the as-cast and rolled LMCs, respectively. These enhancements, although leading to a material having nonremarkable properties *per se* (specific strength/ductility values of the present LMCs are matched by many high strength ductile steels), nonetheless constitute a proof-of-concept demonstration of the improvements that can be achieved by the LMC approach.

"A direct 'rule of mixtures' estimate of the peak homogeneous composite strain (at the onset of necking) computed as the volume average of individual phase peak homogeneous strains is, unlike the Young's modulus or flow stress, not supported by theory.[5–7] Rather, one must conduct a stability analysis on composite deformation, using, for the present composites, the equistrain rule of mixtures. Given that coarse-grained magnesium is relatively strain-rate insensitive,[12,19,20] and given that monolithic materials and the composites were tested at the same strain rate, we ignore for simplicity strain-rate effects, and apply the simple Considere criterion to predict the uniform tensile elongation of the composites from properties of their constituents."

We use, to this end, larger-strain power-law fits[21] of the true-stress/true-strain curves for the two constituent phases to obtain

$$\sigma^{SPCC} = 595.3\,\varepsilon^{0.27} \quad [1]$$

for the SPCC steel sheets, and

$$\sigma^{ZM21} = 355.1\,\varepsilon^{0.16} \quad [2]$$

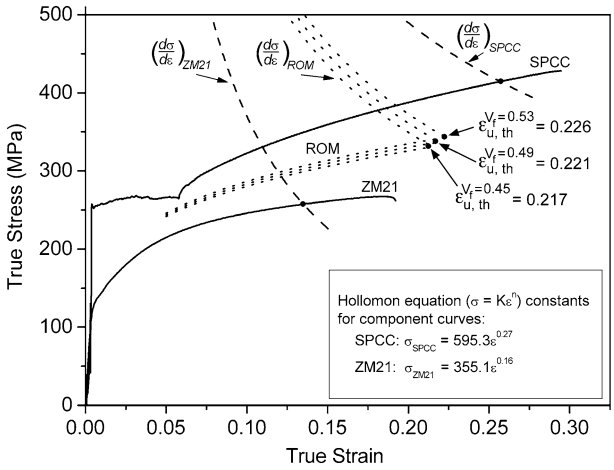

Fig. 8—Considere constructions for the true-stress/true-strain behavior of the constituent phases (ZM21 and SPCC steel) and the equistrain ROM predictions deduced by fitting constituent phase curves with the Hollomon equation (resulting fits are given in the inset; refer to text for details).

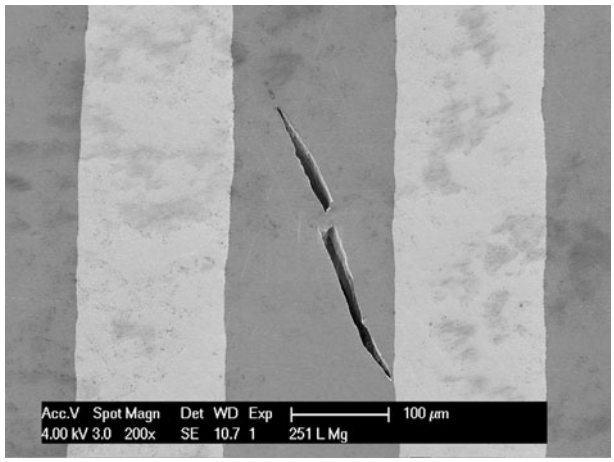

Fig. 9—Cracks inside the ZM21 alloy layers after tensile testing in an area remote from the fracture surface (secondary-electron SEM image; the darker phase is the ZM21 magnesium alloy).

Table V. Vickers Microhardness of the SPCC Steel and ZM21 Alloy Layers in As-Cast and Rolled LMCs

LMC	Component	Load (gf)	Hardness (HV)
As-cast LMC—0.1 mm	SPCC steel	50	234.4 ± 6.8
	ZM21	10	89.5 ± 5.2
Rolled LMC—0.1 mm	SPCC steel	50	340.8 ± 13.8
	ZM21	10	85.1 ± 3.2
As-cast LMC—0.2 mm	SPCC steel	50	204.8 ± 8.0
	ZM21	10	86.2 ± 6.0
Rolled LMC—0.2 mm	SPCC steel	50	348.8 ± 15.5
	ZM21	10	93.7 ± 3.7

HV values are presented as mean ± standard deviation.

for the ZM21 magnesium alloy (neglecting the possible influence of manganese diffusion from the ZM21 alloy into the steel, which will only lower somewhat the volume fraction of Mn precipitate in the alloy). Applying then the Considere construction to the equistrain ROM LMC true-stress/true-strain curve computed using Eqs. [1] and [2], one can then deduce the peak homogeneous strain of the composite at the onset of necking, $\varepsilon_{u,th}$; Figure 8 gives three examples, and values corresponding to each sample tested are given in Table IV. As seen, the predicted true strain at necking varies from 0.217 to 0.226 as V_{SPCC} increases from 0.45 to 0.53. Computing the engineering strain at peak engineering stress from the raw tensile curve data (using a dedicated software routine) and converting this to true strain values for each sample gives experimental strain values at peak engineering stresses reported as ε_u in Table IV. As seen, (1) experimental ε_u values tend, on average, to be somewhat lower than $\varepsilon_{u,th}$; and (2) variations in experimental data exceed variations in $\varepsilon_{u,th}$ caused by the (slight) variations in V_{SPCC}.

In the LMC, thus, the magnesium alloy experiences uniform tensile elongations near 20 pct. This value is not exceptional for ZM21 (which can exhibit a uniform elongation of 25 pct through refinement of the microstructure down to a mean grain size of 9 μm[22]), but is well in excess of what is characteristic of the large-grained as-cast microstructure of the alloy (around 14 pct, Table III). In LMCs, deformation of the less ductile metals is stabilized against necking by the more ductile phase; other modes of failure, however, are also possible. Tunnel cracking is one; in the present instance, this failure mode is unlikely. Indeed, assuming an initial defect size equal to the thickness of the ZM21 layers and a fracture toughness of the 15 *nbsp*; $\mathrm{MPa}\sqrt{\mathrm{m}}$ (characteristic of magnesium alloys[23–25]), for steady-state growth of tunnel cracks within the ZM21 layers, the thickness of ZM21 layers should be larger than at least a centimeter, regardless of whether one adopts the elastic[26] or the shear-lag solution[27] of the crack tunneling problem.[11,28]

Interestingly, in samples tested in tension to failure, far from the fracture surface, one can nonetheless discern a few cracks within the ZM21 layers (Figure 9). Since analysis rules out the possibility of crack tunneling, these are probably shear cracks, resulting from slip incompatibility between the large hexagonal crystals (which deform by glide along the limited number of slip systems characteristic of hexagonal crystals together with twinning (Figure 3)) and the harder and more ductile steel layers.

D. *Mechanical Behavior of Rolled LMCs*

Rolling enhances the strength and decreases the ductility of the infiltrated LMCs (Figure 7). Vickers microhardness measurements within the two phases of the composite, given in Table V, reveal that rolling and subsequent annealing work harden only the steel layers. As mentioned previously, the ZM21 alloy grain structure is refined; however, tensile test data of rolled ZM21 sheets published by Nestler *et al.*[22] indicate that this refinement can strengthen the ZM21 alloy by only up to

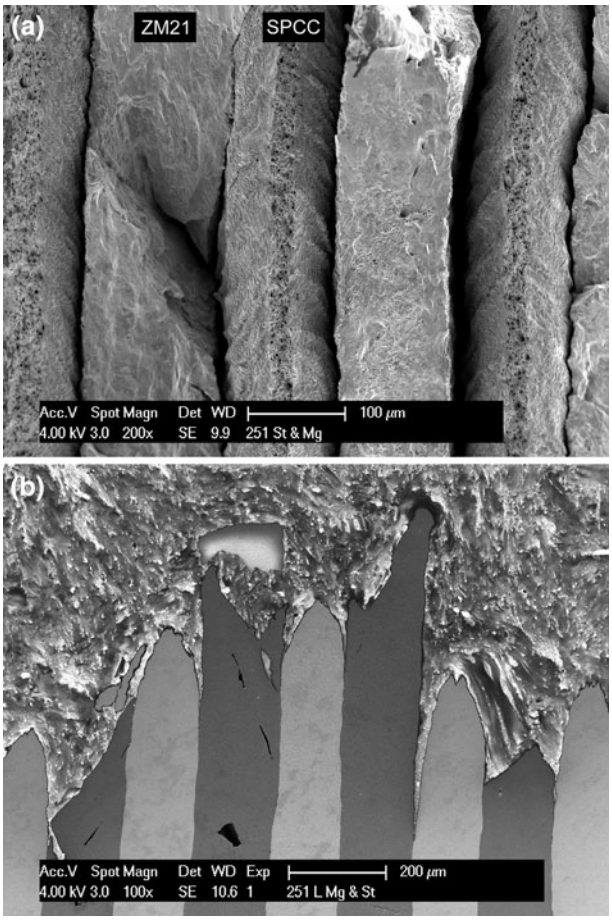

Fig. 10—(*a*) Fracture surface and (*b*) fracture profile of a 0.2-mm as-cast LMC observed in the SEM in secondary electron mode. The light phase is steel and the dark phase is ZM21.

10 MPa. This leads to the conclusion that the rolled LMCs are stronger only because the steel sheets harden by rolling.

E. *Fracture in Infiltrated LMCs*

SEM images of a fracture surface and of a fracture profile of a 0.2-mm as-cast LMC are shown in Figure 10. The steel layers exhibit typical failure by necking followed by ductile fracture by void nucleation, growth, and coalescence. Conversely, the ZM21 alloy fails by shear, without necking. A short zone of delamination, which seems mostly linked to necking of the steel, can be seen between the steel and as-cast ZM21 layers in Figures 10(a) and (b). A closer look at the delaminated surfaces of the as-cast LMCs after fracture (Figure 11) shows the presence of small particles, obviously of manganese, that remain on the surface of the steel layers. This indicates that manganese bonds to steel more strongly than does the primary magnesium phase of the alloy.

SEM images of a fracture surface and of a fracture profile in a 0.2-mm rolled LMC are given in Figure 12. Different from the as-cast samples, there seems to be less void growth in the steel layers, as can be expected given

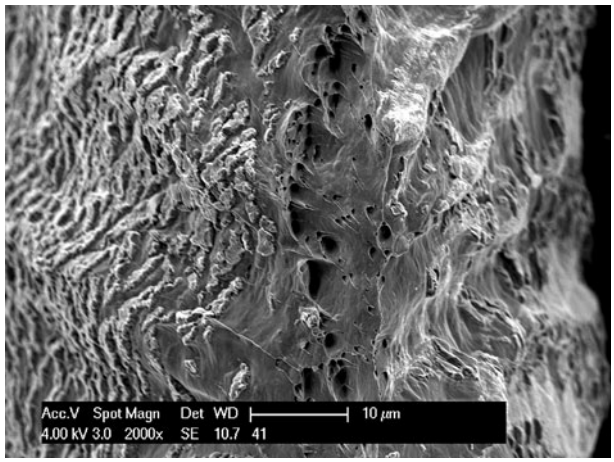

Fig. 11—Close-up of the fracture surface of a steel layer in a 0.2-mm as-cast LMC. On both sides of the wedge, Mn-rich particles are visible. Those particles adhere to steel upon delamination.

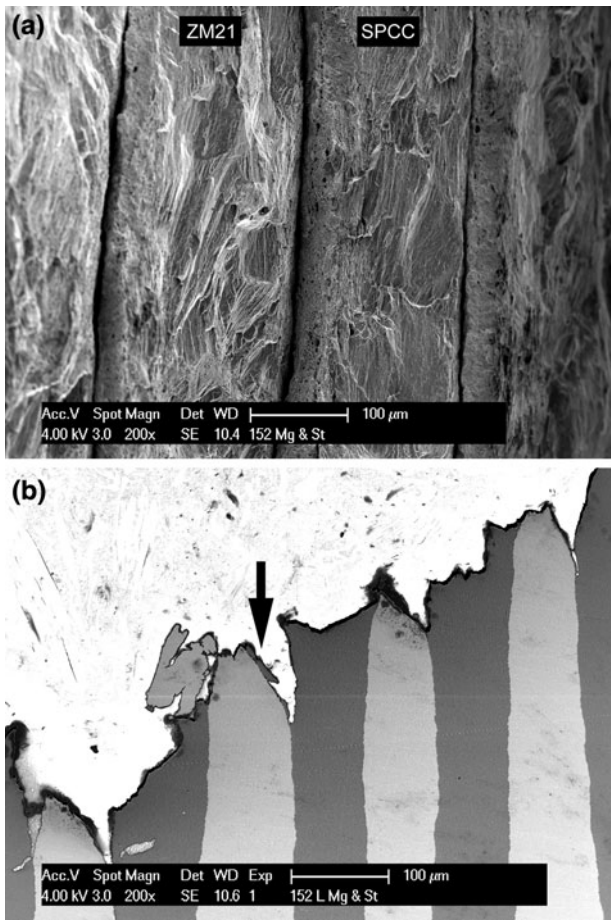

Fig. 12—(*a*) Fracture surface and (*b*) fracture profile of a 0.2-mm rolled LMC observed in the SEM in secondary electron mode. The light phase is steel and the dark phase is ZM21.

the lower strain to failure. Shear striations are visible on fracture surfaces of both components. Fragments of torn ZM21 alloy on fractured steel surfaces

(Figure 12(b), indicated with an arrow) highlight the strength of the interface, which now apparently exceeds the cohesive strength of the ZM21 alloy. This difference between as-cast and rolled samples might result from interfacial roughening, itself creating a certain degree of mechanical interlocking between the steel and magnesium phases.

IV. CONCLUSIONS

Laminated steel–ZM21 alloy composites with layers of 0.2 and 0.1 mm can be produced by infiltration. This is achieved by introducing small dimples in the steel sheets that hold these apart during infiltration. No influence of the dimples was detected in the UTS, proof stress, or (within significant scatter) uniform elongation of the LMCs.

The infiltrated composites are free of pores or intermetallic compounds and show regularly separated metal layers. Manganese in the magnesium alloy segregates to the interface, forming Mn particles there and diffusing into the steel along a band roughly 1-μm wide.

Ultimate tensile strength and uniform elongations of as-cast samples are only slightly lower than equistrain ROM predictions based on tensile curves of individual composite phases processed analogously to phases of the composite. The ZM21 alloy in the as-cast LMCs thus deforms uniformly up to a strain nearly twice that it displays in the absence of steel. Resulting composites can be rolled to a thickness reduction exceeding 50 pct; this work hardens the steel, causing the LMC strength to rise and its ductility to fall, in both cases by a factor of around 2.

ACKNOWLEDGMENTS

This work was sponsored by the Collaborative Research Program between the University of Tokyo and the Ecole Polytechnique Fédérale de Lausanne supported by the Toyota Motor Corporation. The authors are very grateful to the team of the Materials (ATMX) workshop at EPFL, notably to Mr. Werner Brönnimann, for their fine work and helpful advice.

APPENDIX A

Dimpling the steel

The steel sheets were dimpled using a small device including a punch and two aluminum plates (one upper and one lower, Figure A1). The upper plate contains cylindrical holes 1.02 mm in diameter, while the lower plate has matching conical indentations, 1 mm in diameter at the top and 0.5-mm deep. A drawing of the aluminum upper plate is given in Figure A2. Arrangements of dimples in *dimpled* and *nondimpled* specimens are given in Figures A3 and A4, for as-cast and rolled samples, respectively.

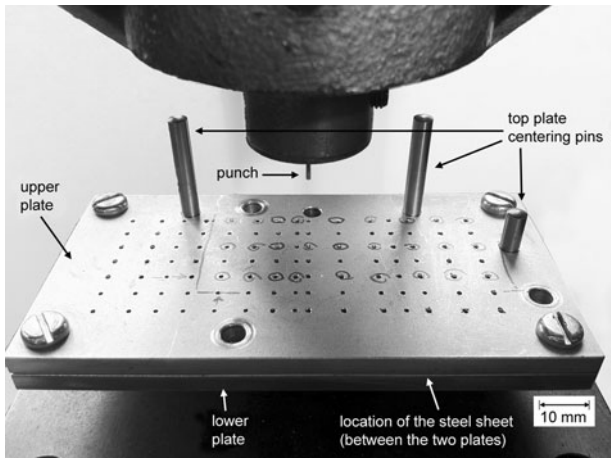

Fig. Al—Photograph of the punching device.

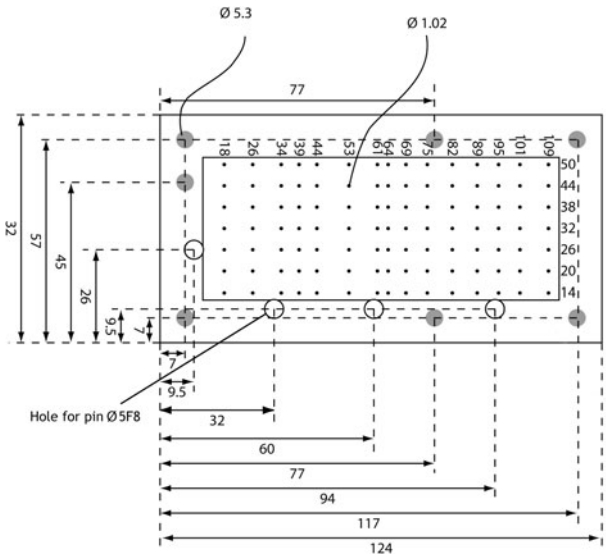

Fig. A2—Aluminum upper plate of the punching device (not to scale). The bottom plate has conical indentations at exactly the same locations with the holes of the upper plate. All dimensions are in millimeters.

APPENDIX B

Assessment of steel sheet stability during infiltration

The resistance to flow of a channel varies as the square of its width: if only for this reason, the molten magnesium alloy is likely to infiltrate the various channels defined between individual steel sheets at different moments. As a result, one side of a steel sheet may be in contact with pressurized molten magnesium alloy while the other side is still under vacuum. This, in turn, will drive the steel sheet to bend.

In order to assess whether this situation will cause the steel sheets to undergo plastic deformation, bending stresses were computed based on elementary linear theory (considering small deflections and linear elasticity). A simple yet realistic one-dimensional geometrical model for the bending of the steel sheets in the present

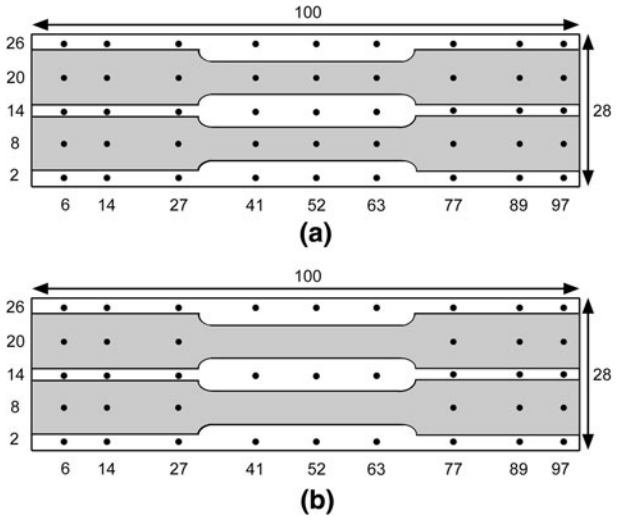

Fig. A3—Arrangements of the dimples used in the production of tensile specimens of as-cast specimens: (*a*) dimpled specimens and (*b*) nondimpled specimens. The tensile samples were machined after infiltration and solidification.

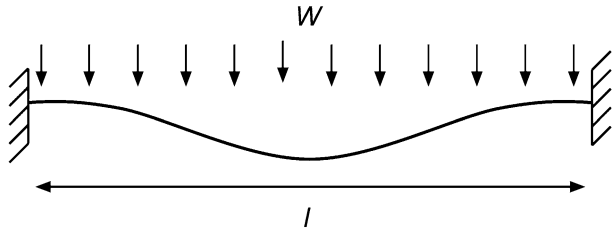

Fig. B1—Illustration of the deformation of a beam fixed at both ends under a uniform load W applied over its entire span.

situation is a rectangular cross-sectional beam under a uniform load W with both ends clamped (Figure B1).

The moment of inertia I of a rectangular cross-sectional beam of width b and thickness t is given by[29]

$$I = \frac{b \cdot t^3}{12} \qquad [B1]$$

The maximum deflection of a beam of length l under a uniform load W (*i.e.*, under uniform applied pressure) with both ends clamped is[29]

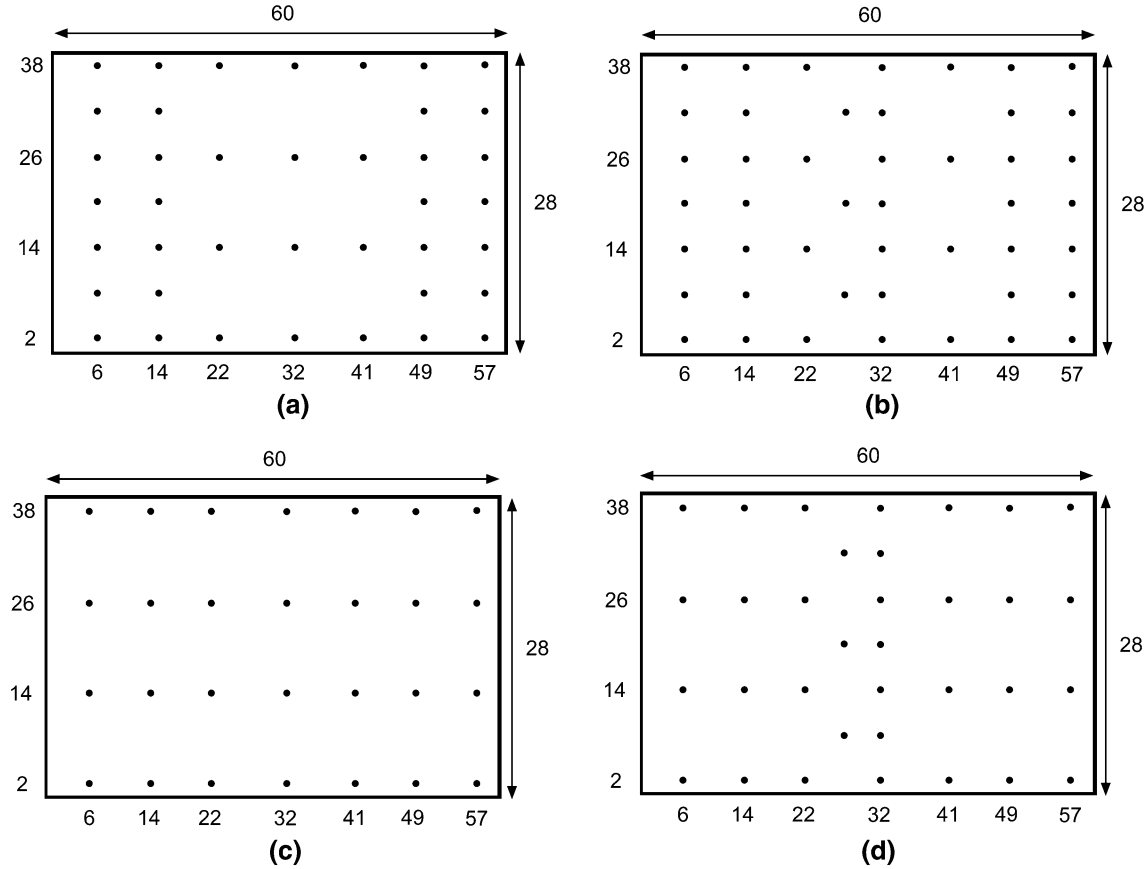

Fig. A4—Arrangement of dimples used in the production of tensile specimens of rolled specimens: with (*a*) 0.1-mm thickness in the nondimpled configuration, (*b*) 0.1-mm thickness in the dimpled configuration, (*c*) 0.2-mm thickness in the nondimpled configuration, and (*d*) 0.2-mm thickness in the dimpled configuration. All dimensions are in millimeters. The tensile specimens were machined after infiltration, solidification, and rolling.

Table B1. Computed Maximum Deflection δ_{max} of the Steel Sheets and the Maximum Stress σ_{max} Imposed on the Steel Sheets During Infiltration

t (mm)	l (mm)	E (MPa)	W (N/mm)	δ_{max} (mm)	σ_{max} (MPa)
0.2	30	1.4×10^5	0.2	4.520	2250
0.2	30	1.4×10^5	0.03	0.678	338
0.1	30	1.4×10^5	0.2	36.161	9000
0.1	30	1.4×10^5	0.03	5.424	1350

Table B2. Required Distance Between Spacers to Maintain the Stress on the Steel Sheets Below the Elastic Limit of Steel (60 MPa)

t (mm)	σ_{max} (MPa)	E (MPa)	W (N/mm)	δ_{max} (mm)	l (mm)
0.2	60	1.4×10^5	0.2	0.002	4.5
0.2	60	1.4×10^5	0.03	0.015	11.5
0.1	60	1.4×10^5	0.2	0.001	2.2
0.1	60	1.4×10^5	0.03	0.007	5.8

$$\delta_{max} = \frac{-W \cdot l^4}{384 \cdot E \cdot I} \text{at } x = \frac{l}{2} \quad [B2]$$

where E is the Young's modulus of the beam.

The maximum stress in the beam is[29]

$$\sigma_{max} = \frac{M_{max} \cdot t}{2 \cdot I} \quad [B3]$$

where the maximum moment M_{max} is given as[29]

$$M_{max} = \frac{-W \cdot l^2}{12} \text{at } x = 0 \text{ and } x = l \quad [B4]$$

The temperature during infiltration was 983 K (710 °C). As a result, both the Young's modulus and the proof stress of steel sheets are reduced compared to room temperature; these are estimated as 140 GPa[30] and 60 MPa,[31] respectively.

The maximum and minimum pressures applied during infiltration were 0.2 and 0.03 MPa, respectively. Table B1 summarizes maximum deflections and bending stresses for these two values, for sheets either 0.2- or 0.1-mm thick, with a free length between spacers equal to 30 mm, corresponding to the gage length of tensile samples. As seen, in either case, bending stresses far exceed the elastic limit of the steel. Predicted deflections generally exceed those admitted by linear theory and also exceed the distance between sheets. Therefore, it is likely that uncontrolled deflection of the steel sheets will occur during infiltration if no additional spacers are used. Preliminary experiments confirmed this; without dimples, composites contain stacked touching layers of steel pushed apart by molten magnesium.

Spacers are thus required in order to prevent uncontrolled bending. Table B2 examines the placement of additional spacers, created for example by dimpling the steel sheets. Here, a maximum allowable bending stress is set, at the elastic limit of the steel (60 MPa), and the maximum free distance between the dimples is computed. Computed deflection values remain well below the distance between the steel sheets. Depending on sheet thickness and loading conditions, distances between dimples have to be below 11 mm down to 2 mm if plastic deformation of the sheets is to be avoided. Dimple spacings used in the present experimental work are near 10 mm: the present computations suggest that the steel sheets bend at the onset of pressurization (*i.e.* at 0.03 MPa), this spacer separation distance being just short enough to avoid bending of 0.2 mm sheets, but not of the 0.1 mm sheets. Experiments show no sign of extensive bending with both steel thicknesses, Figure 1; assumptions used in the calculations are thus apparently conservative.

REFERENCES

1. C.S. Smith: *A History of Metallography*, 1988 paperback ed., MIT Press, Chicago, IL, 1960, pp. 3–65.
2. J. Wadsworth and D.R. Lesuer: *Mater. Charact.*, 2000, vol. 45, pp. 289–313.
3. D.R. Lesuer, C.K. Syn, O.D. Sherby, J. Wadsworth, J.J. Lewandowski, and W.H. Hunt, Jr: *Int. Mater. Rev*, 1996, vol. 41, pp. 169–97.
4. D. Embury and O. Bouaziz: *Annu. Rev. Mater. Res.*, 2010, vol. 40, pp. 213–41.
5. S.T. Mileiko: *J. Mater. Sci.*, 1969, vol. 4, pp. 974–77.
6. S.L. Semiatin and H.R. Piehler: *Metall. Trans. A*, 1979, vol. 10A, pp. 85–96.
7. G. Garmong and R.B. Thompson: *Metall. Trans.*, 1973, vol. 4, pp. 863–73.
8. S. Nambu, M. Michiuchi, Y. Ishimoto, K. Asakura, J. Inoue, and T. Koseki: *Scripta Mater.*, 2009, vol. 60, pp. 221–24.
9. C.K. Syn, D.R. Lesuer, J. Wolfenstine, and O.D. Sherby: *Metall. Trans. A*, 1993, vol. 24A, pp. 1647–53.
10. S. Nambu, M. Michiuchi, J. Inoue, and T. Koseki: *Compos. Sci. Technol.*, 2009, vol. 69, pp. 1936–41.
11. J. Inoue, S. Nambu, Y. Ishimoto, and T. Koseki: *Scripta Mater.*, 2008, vol. 59, pp. 1055–58.
12. H. Westengen and T.K. Aune: in *Magnesium Technology: Metallurgy, Design Data, Applications*, H.E. Friedrich and B.L. Mordike, eds., Springer-Verlag, Berlin-Heidelberg, 2006, pp. 145–204.
13. B.L. Mordike and T. Evert: *Mater. Sci. Eng. A*, 2001, vol. A302, pp. 37–45.
14. J.C. Viala, D. Pierre, F. Bosselet, M. Peronnet, and J. Bouix: *Scripta Mater.*, 1999, vol. 40, pp. 1185–90.
15. M. Sacerdote-Peronnet, E. Guiot, F. Bosselet, O. Dezellus, D. Rouby, and J.C. Viala: *Mater. Sci. Eng. A*, 2007, vols. 445–446, pp. 296–301.
16. F. Yoshida and R. Hino: *J. Mater. Process. Technol.*, 1997, vol. 63, pp. 66–71.
17. C.S. Roberts: *Magnesium and Its Alloys*, John Wiley & Sons, New York, NY, 1960, pp. 57 and 159.
18. E.F. Emley: *Principles of Magnesium Technology*, 1st ed., Pergamon Press, Oxford, United Kingdom, 1966, p. 941.
19. M.A. Thein, L. Lu, and M.O. Lai: *Mater. Sci. Eng. A*, 2010, vol. A528, pp. 239–46.
20. W.J. Kim, H.W. Lee, S.J. Yoo, and Y.B. Park: *Mater. Sci. Eng. A*, 2010, vol. 528, pp. 874–79.
21. M. Selin: *Metall. Mater. Trans. A*, 2010, vol. 41A, pp. 2805–15.
22. K. Nestler, J. Bohlen, D. Letzig, and K.U. Kainer: in *Magnesium Technology*, R.S. Beals, A.A. Luo, N.R. Neelameggham, and M. Pekguleryuz, eds., TMS, Warrendale, PA, 2007, pp. 95–100, CD-ROM.
23. B. Closset: in *Magnesium Technology: Metallurgy, Design Data, Applications*, H.E. Friedrich and B.L. Mordike, eds., Springer-Verlag, Berlin-Heidelberg, 2006, pp. 289–315.
24. H. Somekawa, Y. Osawa, and T. Mukai: *Scripta Mater.*, 2006, vol. 55, pp. 593–96.

25. H. Somekawa and T. Mukai: *J. Alloys Compd.*, 2006, vol. 417, pp. 209–13.
26. Z. Suo: *Appl. Mech. Rev.*, 1990, vol. 43, pp. S276–S279.
27. H.C. Cao and A.G. Evans: *Acta Metall. Mater.*, 1991, vol. 39, pp. 2997–3005.
28. J.W. Hutchinson and Z. Suo: in *Advances in Applied Mechanics*, J.W. Hutchinson and T.Y. Wu, eds., Academic Press Inc., San Diego, CA, 1992, pp. 63–191.
29. R.J. Roark and W.C. Young: *Formulas for Stress and Strain*, 5th ed., McGraw-Hill Book Co., New York, NY, 1975, p. 100.
30. *Metals Handbook*, vol. 1, *Elevated-Temperature Properties of Ferritic Steels*, ASM INTERNATIONAL, Materials Park, OH, 1990, p. 682.
31. *Specification for Structural Steel Buildings*, American Institute of Steel Construction (AISC), ANSI/AISC 360-05, Chicago, IL, 2005, p. 182.